

# A Large-size Precision Measurement Method based on Sub-FOV Calibration Splicing

<sup>1</sup>PHILIP YAMBA, <sup>2</sup>JAMES KWASI QUAISIE, <sup>3</sup>VITUS MWINTERIBO TABIE, <sup>4</sup>ENOCK ASUAKO LARSON,  
<sup>1</sup>ANTHONY AKAYETI, <sup>5</sup>JOSEPH SEKYE-ANSAH, <sup>2</sup>ABDUL-HAMID MOHAMMED

<sup>1</sup>Mechanical Engineering Department, Faculty of Engineering, Tamale Technical University, GHANA

<sup>2</sup>Welding and Fabrication Engineering Department, Faculty of Engineering, Tamale Technical University, GHANA

<sup>3</sup>Mechanical Engineering Department, Faculty of Engineering, Dr. Hilla Limann Technical University, GHANA

<sup>4</sup>Mechanical and Industrial Eng. Department, Faculty of Engineering, University for Development Studies, GHANA

<sup>5</sup>Mechanical Engineering Department, Takoradi Technical University, Takoradi, GHANA

**Abstract:** The size measurement technique is of great significance to large equipment manufacturing in industries such as automobile, aerospace, shipbuilding etc. Vision measurement for a large-size has become a very promising method where calibration of the cameras is the key and the base to obtain satisfactory accuracy. Because of contact in the conventional metrological method which is not robust and precise for large-size measurement, a new non-contact large-size precision measurement method is proposed in this paper based on the splicing of small-field calibrations which realizes the entire field-of-view (FOV) calibration of the measured component using one binocular stereo vision system. According to the FOV of the binocular stereo-vision system, the size of the measured component was divided into sub-FOVs, and each FOV was calibrated by a planar template using Zhang's method. After matching and combing all the sub-sections, the total size of the component could be obtained. A series of experiments were also conducted to verify the precision and effectiveness of the proposed calibration.

**Keywords:** large-size, precision measurement, small-field calibration combination and machine vision.

Received: June 29, 2022. Revised: January 5, 2023. Accepted: February 11, 2023. Published: March 14, 2023.

## 1. Introduction

In industries, such as automobile, aerospace, and shipbuilding, size measurement technique is of great importance to large-size equipment manufacturing and assembling to guarantee the automatic assembly of the manufactured components and dimensions as designed to be accurately measured [1-3]. However, in large-size component production, the great size of the component makes the measurement range too big to completely measure the entire structure using a single instrument on-site [4]. In aerospace and aviation industries for example which require high-precision components, measuring points are not allowed to be marked on the surface of the components hence making this method unsuitable [5]. Furthermore, for deformation prevention before assembly, large-scale components such as wind turbine blades, upper and lower fuselage skins and wings of aeroplanes are clamped onto a bracket thereby partially obstructing the angle of view and region of interest of the metrological devices for taking a surface measurement of these components [6, 7]. Therefore, in large size production and assembly, research on non-contact measurement techniques for surface measurement is important for precision and efficiency [8]. With recent technological advances in computer, CMOS/CCD sensors, image processing, and object-recognition technologies, the

application of machine vision measurement in the industry has been broadly adopted due to its advantage as a non-contact, high-precision, efficient and real-time measurement technology [9-11]. Empirical research works based on machine vision have been done lately on large-size component measurement methods [12-15]. The camera parameters, also known as camera calibration, are necessary for this non-contact vision technology [16]. A pinhole camera model can be used to simulate a camera in the actual world [17]. By using a perspective projection, this model projects points in 3D. There are intrinsic and extrinsic parameters for the camera that need to be recovered [18]. The intrinsic parameters establish the image geometry of the camera, whereas the extrinsic parameters relate the world coordinates to the camera orientation and location [19]. Five terms in the pinhole camera model represent the camera's fundamental parameters. (An additional radial distortion term can represent most non-linearities in cameras.) Both photogrammetry and computer vision have put a lot of effort into calibrating cameras [20]. These works can be grouped into two classifications; one uses a calibration object and the other does not. The first classification was to apply large-size calibration targets or targets with known space relationships, such as planar patterns based on 2 and 3-dimensional planes [21-25]. The second classification is known as the self-calibration method which does not use a

calibration object [15, 26]. With this method, the movement of the camera was in a stationary scene [27]. Based on these Xu et al. [28] presented a technique for camera calibration using a planar mirror to realize the global calibration of the camera clusters with non-overlapping views. Yu et al. [29] suggested a calibration technique that produced a sizable target that encompassed the whole field of view (FOV) of the camera using the junction points of lines. The method, however, disregards camera distortion while creating calibration points, and the resulting calibration points are not properly distributed in the field of view, which affects calibration precision. Carlos Ricolfe-Viala et al. [30] calibrated a trinocular sensor with three wide-angle-lens cameras using a  $5\text{ m} \times 5\text{ m}$  checkerboard template on the floor of the room. Zhang, et al. [31] proposed a calibration method for cameras with wide FOV by combining small objects into a large target based on planar homography [32]. Li et al. [33] merged two tiny objectives into a single large target using a polynomial projective model with a different solution. The smaller targets' design is significantly limited in both situations.

There are other means applied to calibrate the extrinsic parameters up to a scale, such as wide-angle lenses [30], moving of cameras [34], and optical mirrors [35], instead of any special calibration template. However, since a large number of parameters need to be estimated, this method is very susceptible to noise and is often unstable. Furthermore, there are still many problems to get a good combination of accuracy, robustness and online calibration [36]. For example, serious distortion is unavoidable to the wide-angle lens, the coordinate conversion will lead to the loss of accuracy as well as an increase in complexity [37]. Therefore, the primary motivation proposed in this paper is based on the splicing of sub-FOV calibrations, which realizes the entire field-of-view (FOV) calibration of the measured large-size component using a binocular stereo vision system.

## 2. Principle of sub-fov calibration spicing

The calibration of the vision system is to be developed in a mathematical model of the transformation between world points and observed image points resulting from the image formation process. The parameters of the model can be divided into three categories: (1) extrinsic parameters, which describe the relationship between the camera frame and the world frame, including two position parameters and three orientation parameters; (2) intrinsic parameters, which describe the characteristics of the camera including the lens focal length, pixel scale factors, and location of the image centre; and (3) distortion parameters, which describe the geometric non-

linearities of the camera. Among all these parameters, the first category is the most important one for large-size vision measurement. Due to the limitation of the FOV of the cameras, the calibration of the extrinsic parameters should not only be between the camera frame and the world frame in each FOV but also be a relationship model between all the sub-FOVs through calibration. The vision system based on sub-FOV calibration splicing comprises two CCDs (charge-couple device), a moving platform, and some planar templates as shown in Figure 1.

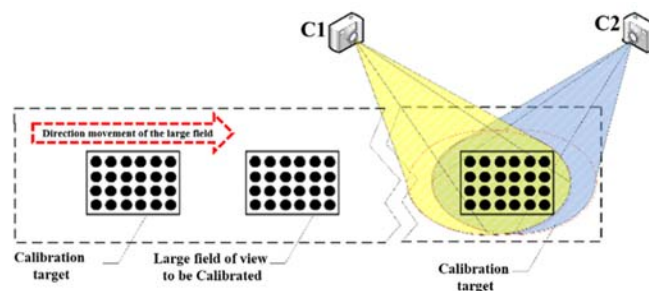


**Fig. 1** Principle diagram of the large-field calibration based on the sub-FOV calibration splicing

Cameras C1 and C2 were composed of a binocular vision system with a set field of view. The intrinsic and extrinsic parameters, as well as the distortion parameters, can be calibrated in this field. The entire FOV of the measured large-size component was divided into sub-FOVs according to the FOV of the binocular vision system with an overlapping view between every two adjacent sub-FOVs. In each sub-FOV, there is a planar template to imitate the pose of the relevant area of the measured workpiece. All the sub-FOVs are moved by the moving platform one after the other into the field of view of the binocular system and are calibrated by applying Zhang's calibration method based on several poses of the planar template [38]. The measured field was divided into several sub-FOVs, the size of each sub-FOV was decided by the field-of-view of the cameras used, the whole large field of view was moved by using a moving platform so that each sub-FOV could go through the camera field-of-view by the order one by one. Beginning from the first sub-FOV, the extrinsic parameters of cameras C1 and C2 are calibrated successively in each sub-FOV through two to three different poses of the template at the same time, and the intrinsic and the distortion parameters are corrected gradually in all the sub-FOVs. The calibration diagram is shown in Fig.2. To get as high calibration accuracy as possible, the following two factors must be noticed: 1) In each sub-FOV, one of the template poses should be similar to that of the relevant position in the measured component, and we choose the first poses here; (2) The changes of the depth of field (DOF) cannot be too much,

as when the focal length is determined the image will blur with the change of DOF to reduce the calibration accuracy.

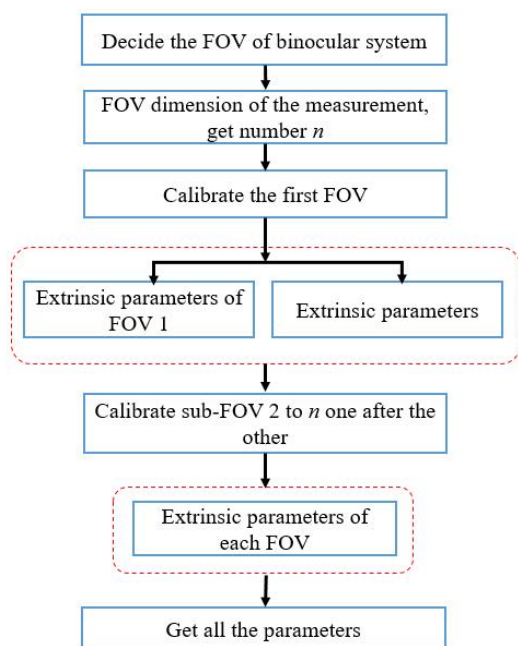


**Fig. 2** Calibration diagram of the large-field calibration based on the sub-FOV calibration splicing

### 3. Experiments and analyses

#### 3.1 Calibration experiment

The experiment setup is composed of two CCDs (charge-coupled device) camera sensors with 1600 pixels  $\times$  1200 pixels, with a pixel size of  $4.65\mu\text{m} \times 4.65\mu\text{m}$ . Two lenses with focal lengths of 12 to 36 mm were selected. A chessboard planar template with an accuracy of 0.02 mm, a precise optic isolation platform and a high-accuracy motor-driven moving platform. The calibration experiment steps are as follows:

(1) the number of sub-FOV according to the field of view of the binocular vision system and the size of the measured component is calculated. In this case, the total field of view of the component is divided into 5 sub-FOVs.

(2) the chessboard is put on the planar template on the first sub-FOV (referred to as calibration position here) and changed with four different poses. An image of each pose by cameras C1 and C2 is taken simultaneously. The extrinsic parameters on the first calibration position are calculated using Zhang's method [38]. The initial intrinsic parameters and distortion parameters of each camera are calculated at the same time.

The physical focal length of the lens can be determined using the camera model [39];

$$f = \frac{1}{2} \left( \frac{f_x}{m_x} \right) + \left( \frac{f_y}{m_y} \right) \quad (1)$$

(3) two images are taken from the second to the fifth calibration position respectively and the extrinsic parameters on each calibration position are calculated. The calculated intrinsic and distortion parameters are gradually corrected by adjustment according to the images on each calibration position. After the above three steps, the extrinsic parameters of each sub-FOV are obtained, and after all these corrections, the accuracy of the intrinsic parameters and distortion parameters are improved. Figure 3 shows the positional relationship between the camera and the template in each sub-FOV. Figure 4 shows a positional relationship between the binocular vision system and the calibration template in each sub-FOV.

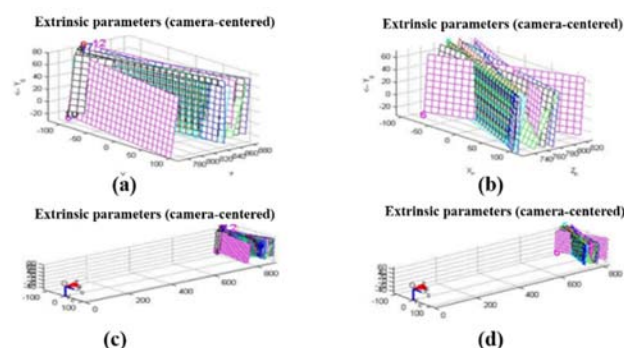


**Fig. 3** Positional relationships between the camera and the template (a) Positions of the template in the left camera C1; (b) positions of the template in the right camera C2; (c) diagram of the extrinsic parameters of the left camera C1; (d) diagram of the extrinsic parameters of the right camera C2

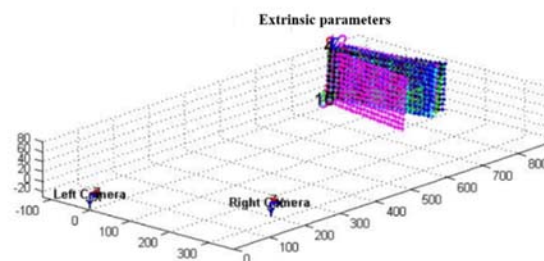


**Fig. 4** Positional relation between the binocular vision system and the calibration template

To evaluate the calibration accuracy, the reprojection errors in each sub-FOV are calculated and shown in Figure 5.

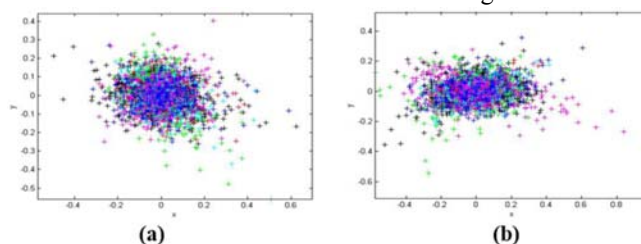


**Fig. 5** Reprojection errors (unit: pixel) (a) Reprojection errors of the left camera C1; (b) reprojection errors of the right camera C2

### 3.2 Analysis

It can be seen from Figure 6 that most of the reprojection errors of cameras C1 and C2 were less than 0.4 pixels which shows that the camera models after calibration by the method based on Sub-FOV Calibration Splicing can describe the imaging relationship of the vision system effectively, that is to say, the calibration accuracy is satisfactory to large-size precision measurement. Nevertheless, there are still some points whose reprojection errors are higher than 0.4 pixels, especially in the pink pose. From Figure 3 and Figure 4, it could be seen that one pink pose was different from the others and there was a big angle between them, which lead to the cause of the calibration error. Furthermore, the printing error of the calibration template, the unstable of the light source etc. may also be a factor causing the calibration errors.

### 3.3 Measurement of large-size cutting tools

After calibration, the vision system is used to measure the cutting tools of a large bending machine with a machining length of 1030 mm. Figure 6 shows the picture of the measurement system.

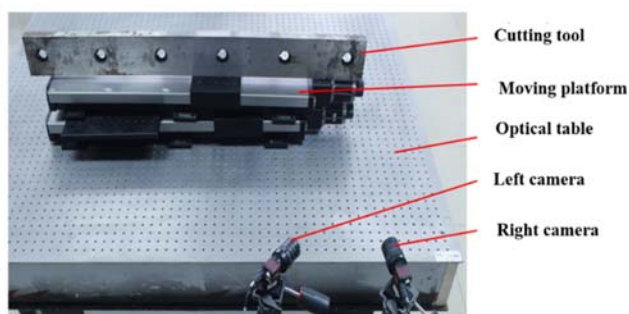


**Fig. 6** Photo of the measurement system

Fig.7 shows the images of each sub-part of one cutting tool in the left camera C1 and the right camera C2 during one measurement process. Here, the letter L means left, that is, the image from the left camera C1 and R means the image from the right camera C2. The number after the dashed line means the number of the subpart, for example, L-2 means the image of the second part is in the left camera C1, the sub-division is shown in Figure 8. The same cutting tool is measured five times, and the results are shown in Table 1.

Before the experiment, the cutting tool was measured by a Coordinate Measuring Machine (CMM) with an accuracy of  $\pm 5\mu\text{m}$ , and the result was 1030.332 mm, which was taken as the true value of the whole length. In Table 1, each measuring error was calculated by each measured whole length minus the

true value of 1030.332 mm. And the relative errors are the measuring errors divided by the true value.

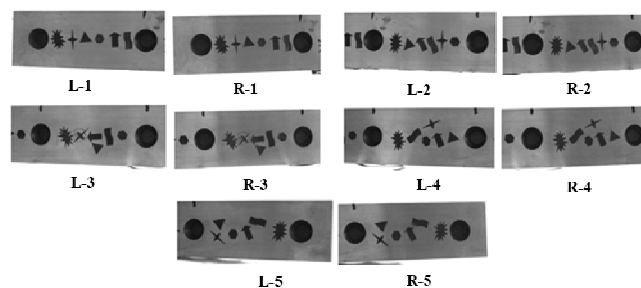


**Fig. 7** images of the sub-parts in the left camera C1 and right camera C2.

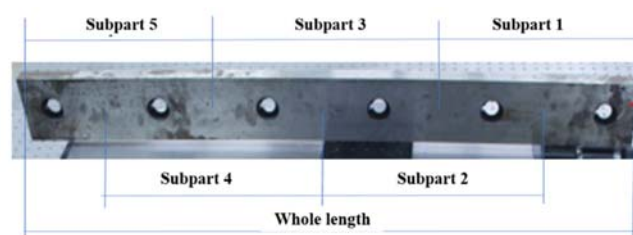


**Fig. 8** Cutting tool divided into 5 sub-FOVs.

**Table 1** Measurement results of the cutting tool with 1030mm length (unit: mm)

|                | 1        | 2        | 3        | 4        | 5        |
|----------------|----------|----------|----------|----------|----------|
| Subpart 1      | 236.354  | 235.959  | 236.615  | 235.777  | 237.029  |
| Subpart 2      | 188.556  | 188.170  | 188.492  | 188.560  | 188.627  |
| Subpart 3      | 187.286  | 187.275  | 187.509  | 187.269  | 187.481  |
| Subpart 4      | 185.210  | 185.042  | 185.389  | 184.962  | 184.974  |
| Subpart 5      | 234.775  | 234.711  | 234.708  | 234.741  | 234.737  |
| Whole length   | 1032.181 | 1031.157 | 1032.713 | 1031.309 | 1032.848 |
| Absolute error | 1.849    | 0.825    | 2.381    | 0.977    | 2.516    |
| Relative error | 0.179%   | 0.080%   | 0.231%   | 0.095%   | 0.244%   |

From Table 1 it can be seen that the highest absolute error was 2.516 mm and the lowest absolute error was 0.825 mm. Again highest relative error was also 0.244% and the lowest relative error was 0.080%. The average relative error was 0.166%. To prove the measurement accuracy of the method based on Sub-FOV Calibration Splicing, four other cutting tools with machining lengths of 1020 mm, 1040 mm, 1050 mm, and 1060 mm were measured, and are shown in Table 2. Here, the data of the 1030 mm cutting tool are the averages in Table 1, and similarly, all the other measured values are also the average of the five measuring results. The results showed that the highest absolute error value was 2.092 mm at a measured length of 1060 mm and the lowest absolute error

value was 1.469 mm at a measured length of 1020 mm. the highest relative error was 0.197% at a measured value of 1060 mm and the lowest value was 0.144% at a measured value of 1020 mm. The true values are all by the same CMM.

**Table 2** Measurement results of different cutting tools (unit: mm)

|                 | 1        | 2        | 3        | 4        | 5        |
|-----------------|----------|----------|----------|----------|----------|
| True value      | 1020.412 | 1030.332 | 1040.023 | 1050.321 | 1060.056 |
| Measured value  | 1021.881 | 1032.042 | 1041.906 | 1052.302 | 1062.148 |
| Absolute error  | 1.469    | 1.71     | 1.883    | 1.981    | 2.092    |
| Relative error  | 0.144%   | 0.166%   | 0.181%   | 0.187%   | 0.197%   |
| Corrected error | -0.023%  | -0.001%  | 0.014%   | 0.021%   | 0.030%   |

From Table 2 it can be seen that all the measured values were larger than those by the CMM. After analysis, it was detected that, because the calibration plane and the measurement plane are not the same, the latter is behind the former, as the template has a certain thickness. According to the projection principle, the measurement plane is bigger than the calibration plane, which will lead to a positive error in the measured value and should be corrected from the measurement results. The correction principle is shown in Figure 9 (a), where  $r$  is the calibration distance from the camera to the calibration plane,  $d$  is the thickness of the template, as well is the distance from the calibration plane to the measuring plane. We can draw the simplified projection model, as shown in Figure 9 (b), where,  $\Delta$  is the absolute error, and  $x$  is the measured size without error by projection.

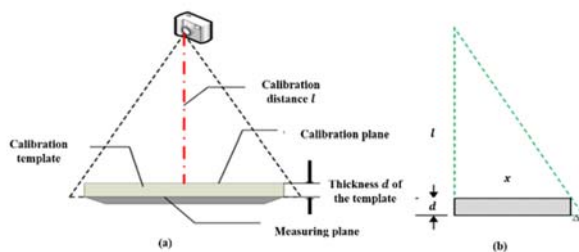


**Fig. 9** Scheme of correction principle (a) Projection principle; (b) simplified projection model

According to the similar triangle principle, the relationship between the parameters is:

$$\frac{\Delta}{x} = \frac{d}{l} \quad (1)$$

So, for each measured size, the correction coefficient  $r$  is:

$$r = \frac{d}{l} \times 100\% \quad (2)$$

In our experiments, the distance from the binocular vision system measured is 601 mm and the thickness of the calibration template is 1 mm, so the correction coefficient is 0.167% according to a similar triangle principle, all the corrected relative errors are shown in Table 2. From Table 2, we can also see that there is some accumulative error in this method, but it can also be corrected.

To further validate the effectiveness of the proposed calibration, therefore, Figure 10 shows the comparison of the experimental results of the binocular vision measurement method based on the traditional two-dimensional image mosaic technology with our present method [38, 40, 41]. To verify the superiority of our method, the measured object is the same metal cutting tool. Because the measurement method based on the traditional 2D image mosaic relies heavily on the accuracy of 2D image mosaic, 2D image mosaic error is very large without distortion correction. It can be seen from Figure 7, in this paper, the measurement results of our proposed method are far superior to the method based on the traditional 2D image mosaic. The resulting error of our method is relatively small as well as high reliability.

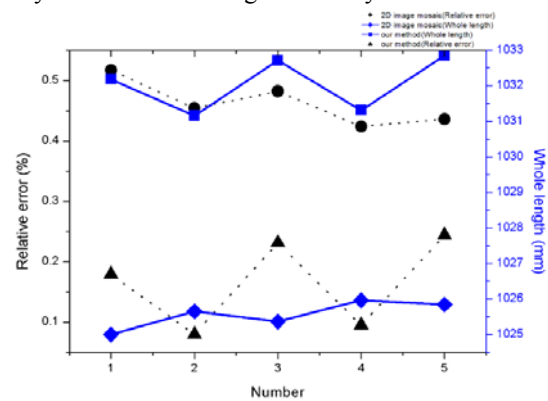


**Fig. 10** Comparison of the experimental results

## 4. Conclusion

In this paper, based on the splicing of sub-FOV calibrations, a new large-size precision measurement method is proposed to realize the whole field-of-view (FOV) calibration of measured large-size workpieces using a binocular stereo vision system. The experimental setup was composed of two CCDs cameras with a resolution of  $1600 \times 1200$ , two lenses with a focal length of 12-36 mm and a resolution of  $1600 \times 1200$ , a chessboard planar template with an accuracy of 0.02mm, a precise optic isolation platform and a high-accuracy motor-driven moving platform. After calibration, this system is applied to measure the cutting tools of a large bending machine. After two images were taken from the second to the fifth calibration position respectively and the extrinsic parameters on each calibration position are calculated.

The calculated intrinsic and distortion parameters were gradually corrected by adjustment according to the images on each calibration position. After the three steps of the calibration experiment, the extrinsic parameters of each sub-FOV were obtained, and after all these corrections, the accuracy of the intrinsic parameters and distortion parameters were improved. Again, the analysis indicated that the reprojection errors of camera C1 and C2 results were less than 0.4 pixels which shows that the camera models after calibration by the method based on Sub-FOV calibration Splicing can describe the imaging relationship of the vision system effectively, that is to say, the calibration accuracy is satisfactory to large-size precision measurement. The measurement results of different cutting tools showed that all the measured values were larger than those by the CMM. Finally, the experiment results show that the measurement accuracy of a workpiece with size 1.02 m -1.06 m is higher than 0.03% after error correction, which can satisfy precision measurement in the industry.

## References

- [1] W. Zhao-hui, D. Ji-wang, Z. Ming-hua, and F. Xiu-min, "Survey on flexible shipbuilding technologies for curved ship-blocks," *Procedia engineering*, vol. 174, pp. 800-807, 2017.
- [2] U. Mutilba, E. Gomez-Acedo, G. Kortaberria, A. Olarra, and J. A. Yagüe-Fabra, "Traceability of on-machine tool measurement: a review," *Sensors*, vol. 17, p. 1605, 2017.
- [3] A. Taşdemir and S. Nohut, "An overview of wire arc additive manufacturing (WAAM) in shipbuilding industry," *Ships and Offshore Structures*, vol. 16, pp. 797-814, 2021.
- [4] C. Andrade and C. Alonso, "Test methods for on-site corrosion rate measurement of steel reinforcement in concrete by means of the polarization resistance method," *Materials and Structures*, vol. 37, pp. 623-643, 2004.
- [5] H. Shang, C. Liu, and R. Wang, "Measurement methods of 3D shape of large-scale complex surfaces based on computer vision: A review," *Measurement*, p. 111302, 2022.
- [6] A. Das, J. M. Sater, C. Crowe, and R. Antcliff, "An assessment of smart Air and space structures: demonstrations and technology," 2000.
- [7] D. R. Gingras, "Experimental Investigation of the Rear-Body Aerodynamics of a Helicopter Fuselage," 2018.
- [8] X. Zou, X. Zhao, G. Li, Z. Li, and T. Sun, "Non-contact on-machine measurement using a chromatic confocal probe for an ultra-precision turning machine," *The International Journal of Advanced Manufacturing Technology*, vol. 90, pp. 2163-2172, 2017.
- [9] Z. Qian, L. Cao, W. Su, T. Wang, and H. Yang, "Recent Advances in Computer Science and Information Engineering: Volume 1," 2012.
- [10] A. Kolb, E. Barth, and R. Koch, "ToF-sensors: New dimensions for realism and interactivity," in *2008 IEEE Computer Society Conference on Computer Vision and Pattern Recognition Workshops*, 2008, pp. 1-6.
- [11] D.-I. B. Hagebeuker and P. Marketing, "A 3D time of flight camera for object detection," *PMD Technologies GmbH, Siegen*, vol. 2, 2007.
- [12] J. Cui, L. Wang, X. Zhao, and H. Zhang, "Towards predictive analysis of android vulnerability using statistical codes and machine learning for IoT applications," *Computer Communications*, vol. 155, pp. 125-131, 2020.
- [13] F. Pecorelli, D. Di Nucci, C. De Roover, and A. De Lucia, "On the role of data balancing for machine learning-based code smell detection," in *Proceedings of the 3rd ACM SIGSOFT international workshop on machine learning techniques for software quality evaluation*, 2019, pp. 19-24.
- [14] M. Sonka, V. Hlavac, and R. Boyle, *Image processing, analysis, and machine vision*: Cengage Learning, 2014.
- [15] W. E. Snyder and H. Qi, *Machine vision* vol. 1: Cambridge University Press, 2004.
- [16] B. Noureddin, P. D. Lawrence, and C. Man, "A non-contact device for tracking gaze in a human computer interface," *Computer Vision and Image Understanding*, vol. 98, pp. 52-82, 2005.
- [17] R. Juarez-Salazar, J. Zheng, and V. H. Diaz-Ramirez, "Distorted pinhole camera modeling and calibration," *Applied Optics*, vol. 59, pp. 11310-11318, 2020.
- [18] A. De la Escalera and J. M. Armingol, "Automatic chessboard detection for intrinsic and extrinsic camera parameter calibration," *Sensors*, vol. 10, pp. 2027-2044, 2010.
- [19] S. De Ma, "A self-calibration technique for active vision systems," *IEEE Transactions on Robotics and Automation*, vol. 12, pp. 114-120, 1996.
- [20] A. Gruen and T. S. Huang, *Calibration and orientation of cameras in computer vision* vol. 34: Springer Science & Business Media, 2013.

- [21] P. Sanmartín, E. Chorro, D. Vázquez-Nion, F. M. Martínez-Verdú, and B. Prieto, "Conversion of a digital camera into a non-contact colorimeter for use in stone cultural heritage: The application case to Spanish granites," *Measurement*, vol. 56, pp. 194-202, 2014.
- [22] A. Cumani and A. Guiducci, "A new camera calibration method for high accuracy non-contact metrology," *Pattern recognition letters*, vol. 14, pp. 415-419, 1993.
- [23] T. D. Alter, "3d pose from 3 corresponding points under weak-perspective projection," MASSACHUSETTS INST OF TECH CAMBRIDGE ARTIFICIAL INTELLIGENCE LAB1992.
- [24] A. Guiducci, "Parametric model of the perspective projection of a road with applications to lane keeping and 3D road reconstruction," *Computer Vision and Image Understanding*, vol. 73, pp. 414-427, 1999.
- [25] S. Gu, C. Lindsay, M. A. Gennert, and M. A. King, "A quick 3d-to-2d points matching based on the perspective projection," in *International Symposium on Visual Computing*, 2008, pp. 634-645.
- [26] T. Cohen and J. Gil, "Self-calibration of metrics of Java methods," in *Proceedings 37th International Conference on Technology of Object-Oriented Languages and Systems. TOOLS-Pacific 2000*, 2000, pp. 94-106.
- [27] O. Masoud and N. P. Papanikolopoulos, "A novel method for tracking and counting pedestrians in real-time using a single camera," *IEEE transactions on vehicular technology*, vol. 50, pp. 1267-1278, 2001.
- [28] Z. Xu, Y. Wang, and C. Yang, "Multi-camera global calibration for large-scale measurement based on plane mirror," *Optik*, vol. 126, pp. 4149-4154, 2015.
- [29] M. Yu, Z. Wei, and J. Sun, "On-spot camera calibration method based on flexible planar target," *J. Univ. Aeronaut. Astronaut. B*, vol. 35, pp. 347-350, 2009.
- [30] C. Ricolfe-Viala, A.-J. Sanchez-Salmeron, and A. Valera, "Calibration of a trinocular system formed with wide angle lens cameras," *Optics express*, vol. 20, pp. 27691-27696, 2012.
- [31] S. Junhua, L. Zhen, and Z. Guangjun, "Camera calibration based on flexible 3D target," *Acta Optica Sinica*, vol. 29, pp. 3433-3439, 2009.
- [32] J. Huo, N. Yang, M. Yang, and J. Cui, "Flexible calibration of camera with large FOV based on planar homography," *Optik*, vol. 126, pp. 5218-5223, 2015.
- [33] W. Li, J. Chu, H. Meng, J. Wang, X. Li, and X. Xing, "Calibration method with separation patterns of a single-camera," in *Ground-based and Airborne Instrumentation for Astronomy*, 2006, pp. 1758-1767.
- [34] K. Kullman, "Experiments with moving children and digital cameras," *Children's Geographies*, vol. 10, pp. 1-16, 2012.
- [35] D. Guerra-Ramos, L. Díaz-García, J. Trujillo-Sevilla, and J. M. Rodríguez-Ramos, "Piston alignment of segmented optical mirrors via convolutional neural networks," *Optics letters*, vol. 43, pp. 4264-4267, 2018.
- [36] C. Antoniou, M. Ben-Akiva, and H. N. Koutsopoulos, "Nonlinear Kalman filtering algorithms for on-line calibration of dynamic traffic assignment models," *IEEE Transactions on Intelligent Transportation Systems*, vol. 8, pp. 661-670, 2007.
- [37] Z. Zhang, Y. Zhou, H. Liu, and H. Gao, "In-situ water level measurement using NIR-imaging video camera," *Flow Measurement and Instrumentation*, vol. 67, pp. 95-106, 2019.
- [38] S. Zhang, B. Li, F. Ren, and R. Dong, "High-precision measurement of binocular telecentric vision system with novel calibration and matching methods," *IEEE Access*, vol. 7, pp. 54682-54692, 2019.
- [39] Z. Wang, Z. Wu, X. Zhen, R. Yang, J. Xi, and X. Chen, "A two-step calibration method of a large FOV binocular stereovision sensor for onsite measurement," *Measurement*, vol. 62, pp. 15-24, 2015.
- [40] S. Guo, S. Chen, F. Liu, X. Ye, and H. Yang, "Binocular vision-based underwater ranging methods," in *2017 IEEE International Conference on Mechatronics and Automation (ICMA)*, 2017, pp. 1058-1063.
- [41] H. Xiang, L. Cheng, H. Wu, Y. Chen, and Y. Gao, "Mobile Robot Automatic Aiming Method Based on Binocular Vision," in *2021 40th Chinese Control Conference (CCC)*, 2021, pp. 4150-4156.